Proceedings World Geothermal Congress 2023
Beijing, China, April 17 – 21, 2023

A novel thermal-hydro-mechanical-chemical coupled pore-scale model for the rock dissolution and fracturing process

Kaituo Jiao[1], Dongxu Han[2*] and Bo Yu[2]

[1]State Key Laboratory of Multiphase Flow in Power Engineering, Xi'an Jiaotong University, Xi'an, 710049, China

[2] School of Mechanical Engineering, Beijing Key Laboratory of Pipeline Critical Technology and Equipment for Deepwater Oil & Gas Development, Beijing Institute of Petrochemical Technology, Beijing 102617, China

*Corresponding author: handongxubox@bipt.edu.cn

Keywords: THMC coupled, rock dissolution, fracturing, LBM-DEM, pore-scale

ABSTRACT

Acid fracturing is one of the primary engineering techniques for improving the connectivity in enhanced geothermal systems (EGS), in which the entire process is a classical thermal-hydro-mechanical-chemical (THMC) process. This paper develops a pore-scale THMC coupled model combined with the lattice Boltzmann method (LBM) and the discrete element method (DEM). Comprehensive THMC coupled phenomena in pore-scale are considered, including fracture dependent fluid conductivity, conjugate heat transfer, hydrodynamic force, thermal strain, rock dissolution, convective transport of heat and solute, chemical damage, etc. The chemical damage variable based on the cohesive bond is proposed to characterize the alteration of mechanical parameters caused by the local rock dissolution. The Lattice Boltzmann (LB) solute transport model combining the volume of pixel (VOP) method is adopted to calculate the change of fluid pathway caused by rock dissolution. After validations, the influence of injected pressure and Damkohler number (Da) on the THMC coupled rock dissolution, and fracturing process is analyzed using the present model. There are three rock dissolution types, i.e., permeation type, cavity type, and permeation-cavity type. For the permeation-cavity type, the dissolution around the main fracture shows the cavity type, while the dissolution around the secondary fractures presents the permeation type. The pattern of the evolution of rock dissolution area with time is also closely related to the rock dissolution type.

1. INTRODUCTION

Enhanced geothermal system (EGS) is an effective method to exploit deep geothermal energy by injecting fluid through underground fracture networks. Due to the high-pressure and high-temperature conditions, fracturing and heat exploitation in EGS is a typical thermal-hydro-mechanical (THM) coupled problem. To further enhance fluid conductivity and improve productivity, acid fracturing has been frequently adopted, which involves solute transport and rock dissolution (H. Xu et al., 2021). CO2 geological sequestration (R. Zhang et al., 2016) and unconventional oil and gas exploitation (Wang et al., 2017) also involve similar engineering conditions. The thermal-hydro-mechanical-chemical (THMC) modeling for the rock dissolution and fracturing process is essential for a better understanding of underlying mechanisms.

Multi-physical coupling models of rock can be divided into macro scale and pore scale. Macro scale models have more engineering value than pore scale models. Characteristic parameters such as porosity, permeability, and diffusivity in macro models are defined at the continuum scale. However, the process leading to the alteration of these parameters often occurs at the pore scale and is closely related to local crack distribution. It is hard to properly understand and describe the changes in these parameters at the continuum scale due to the mismatch in length scales (L. Chen, Kang, Viswanathan, et al., 2014; Kang et al., 2010). To address it, the alteration of these parameters is often coupled by empirical relationships in the calculation, which are obtained from pore-scale simulations or experiments. Hence, pore scale studies are necessary for adequately characterizing these parameters and investigating constitutive relationships among them.

Pore scale and multi-physical modeling consists of two parts: rock mechanics and flow and heat mass transfer. The rock mechanics modeling needs to consider the continuous deformation process when the strain of porous medium is small and the discontinuous deformation process from intact material to fracture initiation and propagation (Krzaczek et al., 2021). It can be divided into two types: continuum-mechanics method and discontinuum-mechanics. The first type is based on the finite element method (FEM) or the extended finite element method (XFEM) (Pathak et al., 2015). The elements around the crack surface should be refined and combine complex non-linear constitutive equations (Lisjak & Grasselli, 2014; W. Zhang et al., 2019). Computation cost is positively correlated with fracture geometry complexity. In comparison, the second type is more suitable for calculating the rock with multiple fractures. Common approaches include discrete element modeling (DEM) and discontinuous deformation analysis (DDA) (Shi & Goodman, 1988). Discontinuum-mechanics requires a small time step, but some large-scale fracture simulations are carried out with the improvement of computer performance (Ji & Tian, 2021). The combination of continuum and discontinuum-mechanics can form complementary advantages, such as the finite element/discrete element coupling method (FDEM).

The flow and heat mass transfer modeling can also be divided into two types. The first is the pore network model (PNM), where the irregular fractures and pores inside rock are simplified as the spherical pores connected by one-dimensional throats (S. Zhou et al., 2017). Fluid is regarded only inside the spherical pores. Heat and mass exchange between pores and interaction between fluid and solid are all calculated by one-dimensional formulas. This type has high computational efficiency, but the application of empirical relations is inevitable (e.g., all the flow is assumed to satisfy Poiseuille or Darcy flow (Krzaczek et al., 2021; W. Li et al., 2016)). Moreover, constructing a reasonable pore network model based on the real core structure is a difficult and key step (Ramstad et al., 2019). The second type has a detailed reconstruction of pore structure. On the basis of describing the pore structure in detail, the Navier-stokes equations are solved only inside the actual pore region. Heat and mass transfer equations are solved based on the flow

velocity in pores. Traditional computational fluid dynamics methods (CFD) have a limited application in pore scale because of the difficulty in dealing with complex irregular fluid-solid geometry. However, the lattice Boltzmann method (LBM) can overcome this difficulty because its underlying kinetic nature makes it effective in complex and moving fluid-solid boundary treatment (Krüger et al., 2016). The meshless method, i.e., smoothed particle hydrodynamics (SPH), also has advantages in dealing with complex fluid-solid boundaries, and it has been applied to the THM coupled simulation (T. Xu, n.d.). Table 1 lists the summarization of the above modeling methods.

Table 1 Pore scale modeling methods in rock

	Modeling type	Numerical methods	Advantages	Disadvantages
Rock mechanics	Continuum-mechanics	FEM, XFEM, etc.	Efficient calculation of continuous and small strain regions	Inapplicably of complex fracture geometry
	Discontinuum-mechanics	DEM, DDA, FDEM, etc.	Discontinuous deformation and large strain simulation	Calibration of contact parameters; High computation cost
Fluid and heat mass transfer	Pore network model	PNM	High computation efficiency	Difficulty in reasonably constructing pore networks
	Detailed reconstruction	CFD, LBM, SPH, etc.	Accurate information on multi-physical fields	High computation cost

The combination of rock mechanics methods and flow and heat mass transfer methods listed in Table 1 can produce a variety of multi-physical models in pore scale. For example, hydro-mechanical (HM) coupled models (Ji & Tian, 2021), thermal-mechanical (TM) coupled models (De Schutter, 2002), and THM coupled models (Caulk et al., 2020; Caulk & Chareyre, 2019). These models are applicable to underground rock fracturing simulation. However, to the authors' knowledge, there are few studies on the coupling of rock mechanics and chemical field, i.e., hydro-mechanical-chemical (HMC) coupled simulation and THMC coupled simulation. The reason is that the fracture pathway and pore structures would change due to rock dissolution, which has a great impact on rock mechanical parameters and fracture propagation (Huang et al., 2021). The rock dissolution process also has a continuous impact on heat and mass transport, which should be paid attention to pore scale. An effective numerical mean to represent the coupling among the mechanical field, chemical field and fracture propagation in pore scale is remained to develop.

In this study, we propose a pore-scale THMC coupled model for the rock dissolution and fracturing process, which is developed based on our previous THM coupled model combing the LBM and DEM (Jiao et al., 2021, 2022). A comprehensive THMC coupled scheme in pore scale is conducted. Especially the chemical damage factor based on the cohesive bond is proposed to characterize the influence of rock dissolution on local mechanical parameters. The Lattice Boltzmann (LB) solute transport model and the volume of pixel (VOP) method are combined to characterize the change of fluid pathway caused by rock dissolution. After validations, the THMC coupled rock dissolution, and fracturing process is preliminarily investigated.

2. PHYSICOCHEMICAL MODEL

2.1 Fluid Flow

For the pore-scale problem, the space inside the rock is divided into solid skeleton and fracture (or pore) (Caulk et al., 2020; L. Chen et al., 2012; Tahmasebi & Kamrava, 2019). The fluid is present only in the fluid pathway induced by the fracture and rock mechanical damage (characterize microscopic defects). Other regions are solid and impermeable. Navier-stokes equations are involved in the fluid pathway, expressed as,

$$\begin{cases} \dfrac{\partial \rho_{\mathrm{f}}}{\partial t} + \nabla \cdot \left(\rho_{\mathrm{f}} \mathbf{u}_{\mathrm{f}} \right) = 0 \\ \dfrac{\partial \left(\rho_{\mathrm{f}} \mathbf{u}_{\mathrm{f}} \right)}{\partial t} + \left(\mathbf{u}_{\mathrm{f}} \cdot \nabla \right) \rho_{\mathrm{f}} \mathbf{u}_{\mathrm{f}} = -\nabla p_{\mathrm{f}} + \nabla \cdot \left(\nabla \mu_{\mathrm{f}} \mathbf{u}_{\mathrm{f}} \right) \end{cases} \tag{1}$$

where ρ_{f} is the fluid density, t is the simulation time, $\mathbf{u}_{\mathrm{f}}$ is the flow velocity, p_{f} is the fluid pressure, and μ_{f} is the dynamic viscosity of fluid.

2.2 Heat Transport

The heat convection-diffusion equation is adopted in the fluid pathway, as presented in Eq. (2). In the solid, heat diffusion equation is involved, as presented in Eq. (3).

$$\frac{\partial T_{\mathrm{f}}}{\partial t} + \left(\mathbf{u}_{\mathrm{f}} \cdot \nabla \right) T_{\mathrm{f}} = \kappa_{\mathrm{f}} \Delta T_{\mathrm{f}} \tag{2}$$

$$\frac{\partial T_{\mathrm{s}}}{\partial t} = \kappa_{\mathrm{s}} \Delta T_{\mathrm{s}} \tag{3}$$

where T_{f} and T_{s} are fluid and solid temperatures, κ_{f} and κ_{s} are fluid and solid thermal diffusion coefficients.

Conjugate heat transfer condition should be satisfied at the fluid-solid boundary, which means that the temperature and the heat flux are continuous on both fluid and solid sides, given by,

$$\begin{cases} T_{\mathrm{f}} = T_{\mathrm{s}} \\ \kappa_{\mathrm{f}} \dfrac{\partial T_{\mathrm{f}}}{\partial n_{\mathrm{s}\to\mathrm{f}}} = \dfrac{\left(\rho c_p\right)_{\mathrm{s}}}{\left(\rho c_p\right)_{\mathrm{f}}} \kappa_{\mathrm{s}} \dfrac{\partial T_{\mathrm{s}}}{\partial n_{\mathrm{s}\to\mathrm{f}}} \end{cases} \tag{4}$$

where c_p is the heat capacity, $n_{\mathrm{s}\to\mathrm{f}}$ is the direction normal to the reactive surface and points from the solid to the fluid.

2.3 Reactive and Transport

It is assumed that the solute concentration has negligible influences on the hydrothermal properties of fluid. The governing equation for solute transport inside the fluid pathway is expressed as,

$$\frac{\partial C}{\partial t} + \nabla \cdot \left(C \mathbf{u}_{\mathrm{f}}\right) = \nabla \cdot \left(D \nabla C\right) \tag{5}$$

where C is the molar concentration of solute, and D is the solute diffusivity.

Rock is a multi-component mixture, and the actual dissolution process involves many interaction reactions. This work emphasizes model building and THMC coupled mechanism analysis, so only one typical reaction is considered here,

$$L1 + S1 \underset{\text{precipitation}}{\overset{\text{dissolution}}{\rightleftharpoons}} L2 \tag{6}$$

where $L1$ is the acid reactant, $S1$ is the dissolved solid, and $L2$ is the product. Eq. (6) can be regarded as a simplified form of several real rock dissolution processes. For example, the limestone ($CaCO_3$) dissolves due to immersion in low PH solution (H^+).

The typical first-order reaction is assumed at the reactive surface, and the related concentration boundary conditions are as follows,

$$\begin{cases} D_{L1} \dfrac{\partial C_{L1,w}}{\partial n_{\mathrm{s}\to\mathrm{f}}} = k_r \left(C_{L1,w} - \dfrac{C_{L2,w}}{K_{\mathrm{eq}}} \right) \\ D_{L2} \dfrac{\partial C_{L2,w}}{\partial n_{\mathrm{s}\to\mathrm{f}}} = -D_{L1} \dfrac{\partial C_{L1,w}}{\partial n_{\mathrm{s}\to\mathrm{f}}} \end{cases} \tag{7}$$

where k_r is the effective forward reaction rate constant, K_{eq} is the effective equilibrium constant, C_{L1} and C_{L2} are the molar concentrations of reactant and product, and subscript w represents that it is on the wall surface having a reaction.

k_r has a positive correlation with local temperature, expressed as,

$$k_r = k_r^0 \exp\left[-\frac{E_a}{R} \left(\frac{1}{T} - \frac{1}{T_0} \right) \right] \tag{8}$$

where T_0 is the reference temperature, k_r^0 is the effective forward reaction rate constant at the reference temperature, E_a is the activation energy, and R is the molar gas constant.

The rock dissolution would cause the change in solid volume, which is calculated by,

$$\frac{\partial V_{S1}}{\partial t} = -A M_{S1} k_r \left(C_{L1,w} - \frac{C_{L2,w}}{K_{\mathrm{eq}}} \right) \tag{9}$$

where V_{S1} is the solid volume, A is the reactive surface area, and M_{S1} is the molar volume of solid. The dissolution of solid volume inside rock has two effects on other physical fields: the first is that it changes the fluid pathway and then influences the fluid flow; the second is that it also changes the local mechanical property and then affects the mechanical behaviors.

2.4 Rock Mechanics

The entire intact rock is divided into discretized but bonded particles for DEM simulation. Through the Lagrangian approach, particle motion is tracked in space and time. The governing equations of particle location and rotation are as follows,

$$\begin{cases} m_p \dfrac{\mathrm{d}^2 \mathbf{x}_p}{\mathrm{d}t^2} = \mathbf{F}^{\mathrm{contact}} + \mathbf{F}^{\mathrm{cohesion}} + \mathbf{F}^{\mathrm{f}\to\mathrm{s}} \\ I_p \dfrac{\mathrm{d}^2 \boldsymbol{\omega}_p}{\mathrm{d}t^2} = \mathbf{T}^{\mathrm{contact}} + \mathbf{T}^{\mathrm{cohesion}} + \mathbf{T}^{\mathrm{f}\to\mathrm{s}} \end{cases} \tag{10}$$

where $\mathbf{x}_p$ and $\boldsymbol{\omega}_p$ are the particle location and rotation, m_p and I_{p} are the particle mass and moment of inertia, $\mathbf{F}^{\mathrm{contact}}$, $\mathbf{F}^{\mathrm{cohesion}}$, and

$\mathbf{F}^{f\to s}$ are contact force, cohesion force, and hydrodynamic force exerted on the particle, respectively, $\mathbf{T}^{contact}$, $\mathbf{T}^{cohesion}$, and $\mathbf{T}^{f\to s}$ are contact torque, cohesion torque, and hydrodynamic torque respectively.

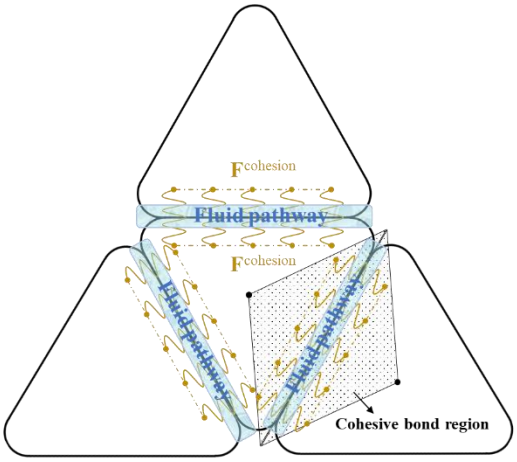

Figure 1: Schematic of cohesive bond.

Cohesive bonds, which induce Fcohesion and Tcohesion, characterize the bonding function inside rock and make the particles into an aggregate. The cohesive bond between two sphero-triangle particles is shown in Figure 1. Fractures and rock mechanical damage are arranged at the cohesive bond to form a fluid pathway. In addition, the strength of the cohesive bond is constrained by the rock strength criterion, expressed as,

$$\left(\frac{\left\langle \sigma_n^c \right\rangle}{\sigma_n^{\mathrm{th}}}\right)^2 + \left(\frac{\sigma_t^c}{\sigma_t^{\mathrm{th}}}\right)^2 \geq 1 \tag{11}$$

where σ_n^c and σ_t^c are the normal and tangential cohesive stresses, σ_n^{th} and σ_t^{th} are the normal and shear cohesive strengths following the Mohr-Coulomb criterion. When Eq. (11) is satisfied, the local rock mechanical damage generates, and it is quantified by the scalar damage variable d_m. The unified linear traction separation law is adopted to represent the constitutive response of d_m (Jiao et al., 2022; Wu et al., 2020), as presented in **Figure 2**. With the increase of d_m, the fluid conductivity of the related cohesive bond would enhance due to the increase of microscopic defects(Jiao et al., 2022). Once d_m increases to 1, the bond failure happens, and the fracture generates, then the fluid conductivity of the related cohesive bond increases to maximum.

Moreover, d_m would degrade the elastic moduli of cohesive bonds, given by,

$$\begin{cases} M_n' = (1-d_m)M_n \\ M_t' = (1-d_m)M_t \end{cases} \tag{12}$$

where M_n and M_t are normal and tangential elastic moduli of cohesive bond.

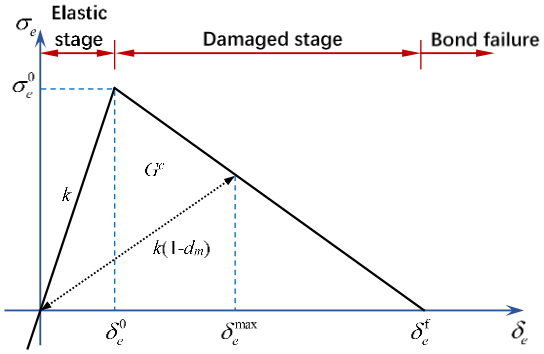

Figure 2: Constitutive response of unified linear traction separation law, where σ_e is equivalent stress and δ_e is equivalent deformation.

In summary, the THMC coupled phenomena considered in our pore-scale model are summarized in Figure 3. Comprehensive THMC coupled phenomena are considered, and there is at least one key coupled phenomenon between every two fields.

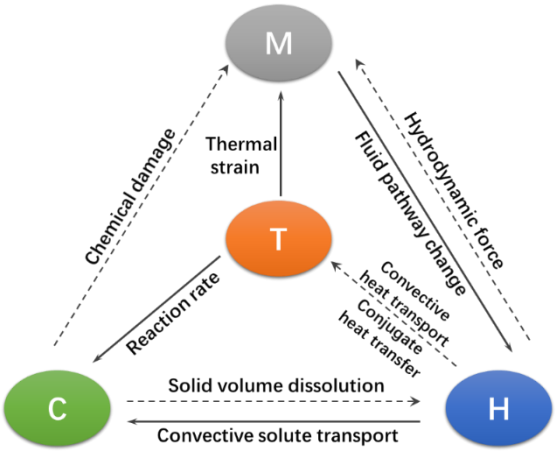

Figure 3: THMC coupled relation during rock dissolution process.

2.5 Problem Description

The rock specimen used for mechanism analysis of THMC coupled rock dissolution process is shown in **Figure 4(a)**. It has a size of 10 cm×7 cm and is discretized as an assembly of sphero-triangle particles. An elaborate design is conducted for the particle size, giving attention to both grid dependency and computation cost(Jiao et al., 2022). Tectonic stresses $\sigma_x = 5.0$ MPa and $\sigma_y = 7.5$ MPa are applied to the outer boundary of rock. The high-pressure ($P_{f,in}$) and low-temperature ($T_{f,in}$) fluid with a high concentration of acid reactant ($C_{L1,in}$) is injected into an injection hole at the left boundary. The left outer boundary is no-flux condition and thermal adiabatic. Other regions of the outer boundary are outflow boundary conditions and maintained at low pressure with $P_{f,out}$=100 kPa. At the initial time, the fluid pressure inside rock is also $P_{f,out}$, the rock temperature is uniform with ΔT=200 ℃, and there is no reactant and product inside rock. A pre-existing fracture adjacent to the injection hole is set to guide the subsequent fracturing.

The mechanical parameters of rock are similar to limestone and sandstone. There are three kinds of $P_{f,in}$ (10 MPa, 20 MPa, 30 MPa) at the injection hole to obtain different intensities of convection in the rock dissolution process. The temperature of the injection fluid is maintained at 15 ℃. Various Damkohler numbers (1.5×10^{-5}, 1.5×10^{-3}, 1.5), which stands for the ratio between reaction and diffusion, are adopted for investigating the influence of reaction intensity,

$$Da = \frac{k_r^0 l_c}{D_{L1}} \tag{13}$$

where Da is Damkohler number, l_c is the characteristic length defined as the width of rock. k_r^0 is obtained by the value of Da. It is assumed that the rock has only one kind of mineral, i.e., $S1$. The rock has an initial porosity of 0.15, so it has initial permeability. To represent the initial permeability, the initial flow pathway is set at cohesive bonds as shown in **Figure 4(b)**, which is a common way in pore-scale simulation (Boutt et al., 2011; Z. Chen & Wang, 2017). Other necessary calculated parameters and property parameters are given exactly after the presentation of numerical method (Section 4).

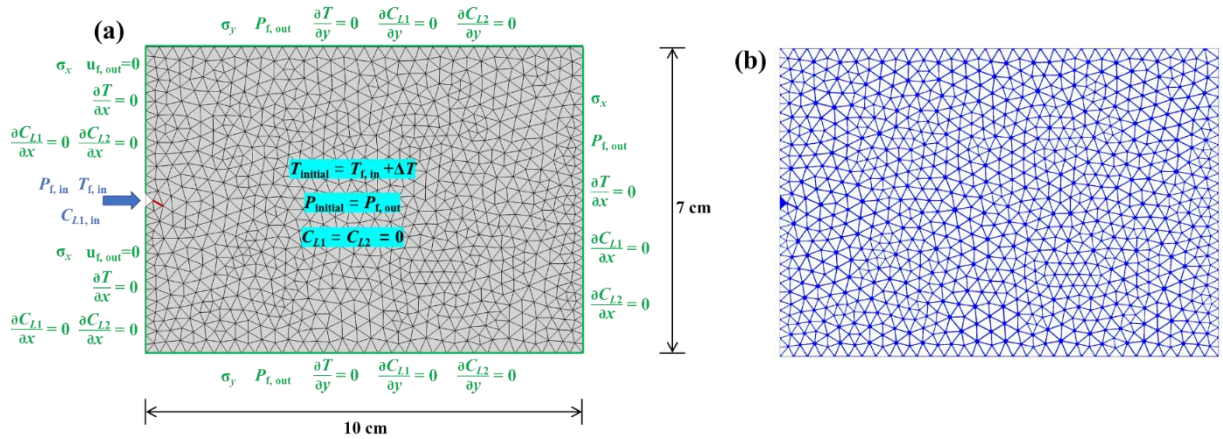

Figure 4: (a) Computation domain and boundary conditions for THMC coupled rock dissolution process. (b) Initial fluid pathway for rock with an initial porosity of 0.15.

3. NUMERICAL METHOD

3.1 LBM-DEM Model for THM Coupling

In our previous work (Jiao et al., 2021, 2022), a pore-scale THM coupled model for fracture propagation process was developed by combing the LBM and DEM. The LB model with multiple relaxation time (MRT) is used to accurately solve the fluid flow in fractures

and heat transport in the entire rock. The DEM based on sphero-triangle particles is adopted to solve the mechanical behaviors inside the rock.

This model considers a comprehensive THM coupled phenomena displayed in **Figure 3**, i.e., convective heat transport, conjugate heat transfer, hydrodynamic force, and thermal strain. Convective heat transport is satisfied intrinsically by two population approach. Conjugate heat transfer is conducted by discretizing Eq. (4) in the lattice grid using temperature distribution function. Hydrodynamic force is calculated by the momentum exchange of pressure distribution function along the fluid-solid boundary. Thermal strain is calculated by the deformation of sphero-triangle particle based on the principle of minimum potential energy. Furthermore, the DEM particles are covered by a much-dense lattice mesh, and there are at least three grids for the aperture of fluid pathway of the cohesive bond. When the rock mechanical damage and fracture generate, the lattice nodes adjacent to fluid pathway would transform from the solid status into the fluid status to increase the fluid conductivity. This enhancement corresponds to the fracture-dependent flow conductivity and is determined by the characteristic factor of fracture fluid pathway c_d (Jiao et al., 2022; Yan et al., 2022).

The THMC coupled model proposed in this paper is developed based on our previously THM coupled model. Solute transport, solid volume dissolution, and chemical damage are new factors to be considered. Therefore, The numerical means on how to represent them will be explained in detail below. Other technical details refer to our previous work (Jiao et al., 2021, 2022).

3.2 LB Model for Solute Transport

For general fluids, solute diffusivity is smaller than kinematic viscosity and thermal diffusion coefficient, making the relaxation parameter of LB model smaller. The LBM would lose numerical stability if the relaxation parameter is too small. Fortunately, the lattice kinematic scheme (LKS) provides a greater range of acceptable diffusivity because it has an adjustable factor for the conversion between diffusivity and relaxation parameter (Meng & Guo, 2016; Sullivan et al., 2005). Its evolution and equilibrium distribution equations are written as,

$$h_i^k(\mathbf{x}+\mathbf{c}_i\delta_t, t+\delta_t) = h_i^k(\mathbf{x},t) - \frac{1}{\tau_h^k}\left[h_i^k(\mathbf{x},t) - h_i^{k,\mathrm{eq}}(\mathbf{x},t)\right] \tag{14}$$

$$h_i^{k,\mathrm{eq}} = w_i H^k\left[1+\frac{\mathbf{c}_i\cdot\mathbf{u}}{c_s^2}+\frac{(\mathbf{c}_i\cdot\mathbf{u})^2}{2c_s^4}-\frac{\mathbf{u}^2}{2c_s^2}\right]+w_i\tau_B^k\delta_t\left(\mathbf{c}_i\cdot\nabla H^k\right) \tag{15}$$

where h_i^k is the concentration distribution function with discrete velocity $\mathbf{c}_i$ at the location $\mathbf{x}$ and time t for the solute k (k =$L1$ or $L2$), τ_h^k is the relaxation parameter, $h_i^{k,\mathrm{eq}}$ is the equilibrium distribution function, w_i is the weight coefficient, H^k is the lattice concentration, $\mathbf{u}$ is the lattice velocity of fluid, c_s is the lattice speed of sound, τ_B^k is the adjustable factor, δ_t is the lattice time step. The discrete velocity $\mathbf{c}_i$ and weight coefficient w_i for the two-dimensional nine-velocity model is given by,

$$\mathbf{c}_i = \begin{cases} (0,0) & i=0 \\ \left(\cos\left[\dfrac{(i-1)\pi}{2}\right],\ \sin\left[\dfrac{(i-1)\pi}{2}\right]\right) & i=1-4 \\ \sqrt{2}\left(\cos\left[(i-5)\pi/2+\pi/4\right],\ \sin\left[(i-5)\pi/2+\pi/4\right]\right) & i=5-8 \end{cases} \tag{16}$$

$$w_i = \begin{cases} \dfrac{4}{9}, & i=0 \\ \dfrac{1}{9}, & i=1-4 \\ \dfrac{1}{36}, & i=5-8 \end{cases} \tag{17}$$

The local concentration gradient in Eq. (15) is calculated by the following equation,

$$\nabla H^k = \frac{\sum_{i=0}^{8}\mathbf{c}_i\left[h_i^k(\mathbf{x},t) - h_i^{k,\mathrm{eq}}(\mathbf{x},t)\right]}{c_s^2\left(\tau_B^k-\tau_h^k\right)\delta_t} \tag{18}$$

According to the Chapman-Enskog expansion, Eq. (14) can recover to Eq. (5). The solute diffusivity in lattice units has a relation with relaxation parameter τ_h^k and the adjustable factor τ_B^k, having,

$$D_k = c_s^2\left(\tau_h^k - \frac{1}{2} - \tau_B^k\right)\delta_t \tag{19}$$

The macroscopic concentration is calculated by,

$$C_k = \sum_{\alpha=0}^{8} h_i^k \tag{20}$$

There is dissolution reaction at the reactive surface, i.e. Eq. (6), and the reactive boundary condition described by Eq. (7) should be involved. In this model, the halfway bounce back scheme is employed (T. Zhang et al., 2012), in which the concentration gradient at the reactive surface is expressed with the difference scheme,

$$\frac{\partial C_w}{\partial n_{\mathrm{s}\to\mathrm{f}}} = \frac{C_f - C_w}{0.5\delta_x} \tag{21}$$

where δ_x is the lattice length, and C_f is the concentration at the fluid node neighboring the surface.

Substituting Eq. (21) into Eq. (7), the concentrations of solute at the surface are obtained as,

$$\begin{cases} C_{L1,w} = \dfrac{2C_{L1,f}D_{L1}D_{L2}K_{\mathrm{eq}} + \left(C_{L1,f}D_{L1} + C_{L2,f}D_{L2}\right)\delta_x k_r}{2D_{L1}D_{L2}K_{\mathrm{eq}} + D_{L1}\delta_x k_r + D_{L2}\delta_x K_{\mathrm{eq}} k_r} \\ C_{L2,w} = \dfrac{K_{\mathrm{eq}}\left[2C_{L2,f}D_{L1}D_{L2} + \left(C_{L1,f}D_{L1} + C_{L2,f}D_{L2}\right)\delta_x k_r\right]}{2D_{L1}D_{L2}K_{\mathrm{eq}} + D_{L1}\delta_x k_r + D_{L2}\delta_x K_{\mathrm{eq}} k_r} \end{cases} \tag{22}$$

After that, the unknown concentration distribution functions at the fluid node neighboring the surface can be calculated as,

$$h_{\bar{i}}^k(\mathbf{x}_f, t+\delta t) = -h_i^{k,*}(\mathbf{x}_f, t) + 2w_i C_{k,w} \tag{23}$$

where $\mathbf{x}_f$ is the location of lattice node neighboring the surface, and superscript * means the collision value of lattice node. It should be noted that Eq. (23) does not consider the movement speed of reactive surface because the rock is approximately static, and the particle motion is very slight.

The solid volume of each lattice node is updated by the VOP method (L. Chen, Kang, Carey, et al., 2014). Each pixel, also lattice node, is assigned a solid volume, and the change of volume is calculated by the time forward difference of Eq. (9), written as,

$$V_{S1}\left(t+\delta_t\right) = V_{S1}\left(t\right) - AM_{S1}k_r\left(C_{L1,w} - \frac{C_{L2,w}}{K_{\mathrm{eq}}}\right)\Delta t_{\mathrm{LBM}} \tag{24}$$

V_{S1} reaches zero means that this lattice node is absolutely dissolved and should become a new fluid node. In order to carry out the simulation normally, initialization information of these new dissolved nodes should be provided. Referring to previous research (L. Chen, Kang, Viswanathan, et al., 2014; X. Zhou et al., 2020), zero velocity and average values of pressure and concentration of the nearest neighbor fluid nodes are set in this model. In addition, rock mechanical damage and fracture generation also involve the transformation of lattice node status from solid to fluid. The difference from the treatment of new dissolved nodes is that the original solid volume of the lattice node would be attached to other solid nodes of the related particle, which can ensure the mass conversation of solid. Furthermore, the influence of particle motion on V_{S1} of each lattice node (Eulerian coordinates) is neglected because the particle displacement is small and inapparent. The variation of V_{S1} also changes the mass of the related particle, so the mass of particle needs to be updated after each LBM time step.

3.4 Chemical Damage Variable

Solid dissolution has a significant effect on pore structure modification and changes the mechanical properties of rock (Huang et al., 2021). The fracture propagation characteristics also have significant changes caused by the variation of mechanical properties (Shovkun & Espinoza, 2019). To capture these features, previous researchers defined chemical damage parameter based on computer tomography (CT) number to quantify the degree of rock dissolution (Y. Chen et al., 2021; S. Li et al., 2018). Then, they discussed the relationship between chemical damage parameter and rock properties. The essence of this parameter is the ratio of dissolved mass to original rock mass. According to this point, we defined a chemical damage variable based on cohesive bond,

$$d_c = 1 - \frac{m_c}{m_c^0} \tag{25}$$

where d_c is the chemical damage variable, m_c is the mass of solid inside the region of cohesive bond (see **Figure 1**), m_c^0 is the value at the initial time. When solid dissolution occurs in the region of cohesive bond, the corresponding d_c will increase.

Accordingly, the comprehensive rock damage variable based on cohesive bond is expressed as,

$$d' = d_m + d_c - d_m d_c \tag{26}$$

where d' is the comprehensive rock damage variable under the coupling effect of mechanical damage and chemical damage.

Bringing d' into Eq. (12) can reflect the influence of chemical damage on elastic modulus. In addition, d_c has a functional relationship with normalized strength parameters and critical fracture energy of cohesive bond,

$$\begin{cases} \dfrac{\sigma_n^{\mathrm{th}}}{\sigma_n^{\mathrm{th},0}} = \dfrac{\sigma_t^{\mathrm{th}}}{\sigma_t^{\mathrm{th},0}} = f_1(d_c) \\ \dfrac{G_{\mathrm{I}}^c}{G_{\mathrm{I}}^{c,0}} = \dfrac{G_{\mathrm{II}}^c}{G_{\mathrm{II}}^{c,0}} = f_2(d_c) \end{cases} \tag{27}$$

where $\sigma_n^{\mathrm{th},0}$ and $\sigma_t^{\mathrm{th},0}$ are strengths of cohesive bond at the initial time, G_{I}^c and G_{II}^c represent the critical fracture energies in pure modes I and II, $G_{\mathrm{I}}^{c,0}$ and $G_{\mathrm{II}}^{c,0}$ are values at the initial time, f_1 and f_2 are empirical functions which are determined by the experimental results.

In summary, the solving process of the proposed THMC model is presented in **Figure 5**.

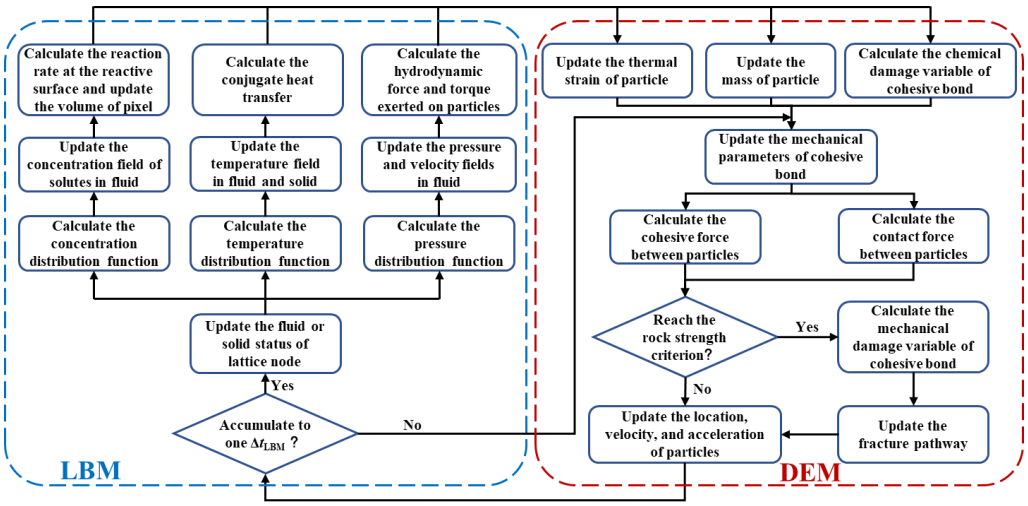

Figure 5: Calculation process of the proposed THMC coupled LBM-DEM pore-scale model.

3.5 Validations

For our LBM-DEM model, THM coupled phenomena have been comprehensively validated in our previous work (Jiao et al., 2021). They are single particle sedimentation for fluid-solid coupling, square thermal expansion for thermal-solid coupling, and thermal cracking for fracture propagation. Hence, this work focuses on the validations of chemical field, i.e., solute transport and chemical damage.

3.5.1 Diffusion-reaction Problem

The solute diffuses in a rectangular cavity with a size of $L \times H$, as shown in **Figure 6(a)**. The solute enters the region from the left boundary with a constant concentration C_{in} and is consumed by the reaction at the top boundary. Right and bottom boundaries are no-flux conditions. Introducing $Da = \dfrac{k_r H}{D}$ and dimensionless concentration $\Psi = \dfrac{C - C_{\mathrm{eq}}}{C_{\mathrm{in}} - C_{\mathrm{eq}}}$, the analytical solution is expressed as,

$$\Psi(x, y) = \sum_{n=0}^{\infty} \frac{\sin(\beta_n H)}{N_n^2 \beta_n} \frac{\cosh\left[\beta_n (x - L)\right]}{\cosh(\beta_n L)} \cos(\beta_n y) \tag{28}$$

where $N_n^2 = \dfrac{H}{2}\left(1 + \dfrac{\sin(2\beta_n H)}{2\beta_n H}\right)$, and $\beta_n H \tan(\beta_n H) = Da$.

Equation (28) indicates that if lengths L and H are given, Ψ is only related to Da. In this case, the computation domain is meshed by 100×80 lattice grids. The diffusion coefficient D is assigned as 0.03, and the adjustable parameter τ_B is assigned as 0.01. **Figures 6(b)** and **6(c)** show the contours of Ψ at situations of Da=4.8 and Da=48. The numerical results agree well with the analytical solutions. Hence, the proposed model and in-house code can correctly simulate the solute transport and reaction process.

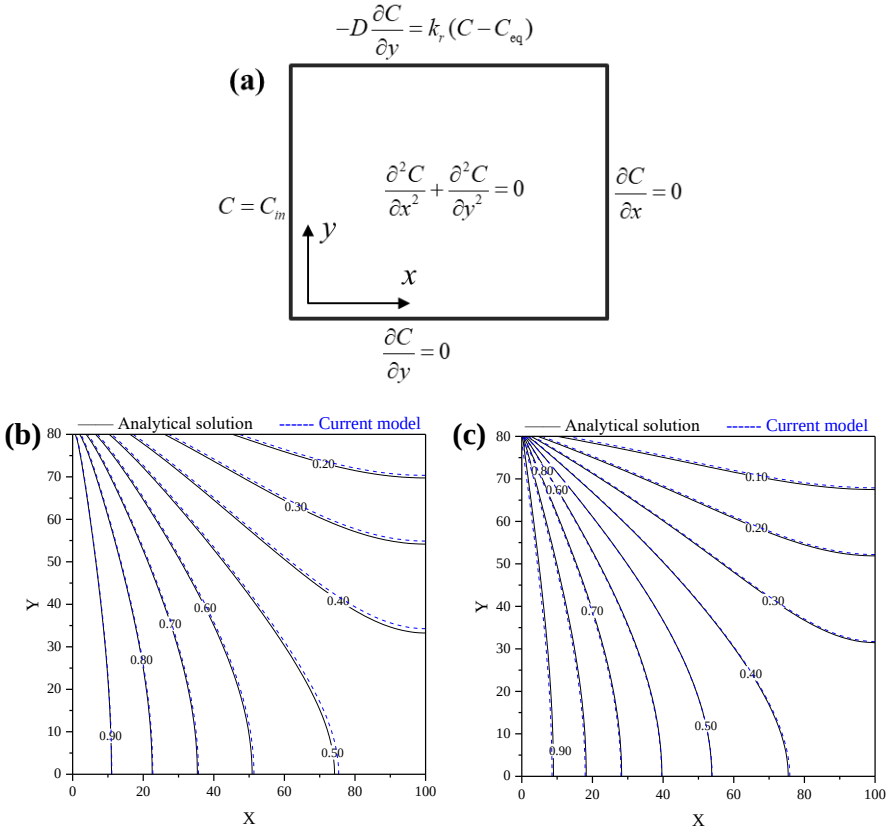

Figure 6: Validation of diffusion-reaction problem. (a) Computational domain and boundary conditions. (b) Contours of dimensionless concentration with *Da*=4.8. (c) Contours of dimensionless concentration with *Da*=48.

3.5.2 Uniaxial Compression of Acid-corroded Sandstone

The results of acid-corroded sandstone under uniaxial compression conducted by Li et al. (S. Li et al., 2021) are adopted to verify the simulation of chemical damage. Their results are also used to verify damage constitutive model (Jin et al., 2021). In the test, they used a group of cylindrical sandstone samples soaked in acidizing fluid (pH=1) for up to 180 days. Each sample had a height of 10 cm and a diameter of 5 cm. Every 30 days of dissolution, they took one sample from the group for weighting and measured its mechanical properties through the uniaxial compression test. The mechanical parameters of uncorroded rock in their test were elastic modulus 27.8GPa and compression strength 91.1MPa. The rock sample is discretized as 2D particles for simulation, as shown in **Figure 7(a)**. Accordingly, after the calibration of numerical tests, the DEM mechanical parameters used for simulation are listed in **Table 1**.

Table 1 DEM mechanical parameters.

Parameter	Value
Density	2500 kg/m^3
Normal spring stiffness	3.73×10^{10} N/m
Tangential spring stiffness	1.69×10^{10} N/m
Normal elastic modulus	24.03 GPa
Tangential elastic modulus	10.68 GPa
Sliding friction coefficient	0.30
Internal friction coefficient	0.47
Damping coefficient in normal contact	1.17×10^3 N·s/m
Damping coefficient in tangential contact	0 N·s/m
Damping coefficient in cohesion	4.60×10^{-6} s/m
Shape parameter of Weibull distribution	7
Normal cohesive strength *	15.0 MPa
Internal cohesion *	95.0 MPa

Critical fracture energy in mode I *	20 N/m
Critical fracture energy in mode II *	64 N/m
DEM time step Δt_{DEM}	2.86×10^{-9} s

* represents the mean value of Weibull distribution

The acid corrosion distribution inside the rock in their experiment was unavailable. Therefore, the equal value of the chemical damage variable is assigned to all cohesive bonds in the computation domain (Jin et al., 2021). This value is estimated by the reduction of elastic modulus in their test results. After that, the relationships between normalized strength parameters and chemical damage variable, critical fracture energies, and chemical damage variable are obtained by fitting test results,

$$\begin{cases} \dfrac{\sigma_n^{\text{th}}}{\sigma_n^{\text{th},0}} = \dfrac{\sigma_t^{\text{th}}}{\sigma_t^{\text{th},0}} = -0.83d_c^2 + 0.017d_c + 0.98 \\ \dfrac{G_{\text{I}}^c}{G_{\text{I}}^{c,0}} = \dfrac{G_{\text{II}}^c}{G_{\text{II}}^{c,0}} = 5.29d_c^2 - 3.34d_c + 1.01 \end{cases} \tag{29}$$

Apply Eq. (29) to our proposed model, and perform uniaxial compression calculations based on the assembly of particles in **Figure 7(a)**. The test results of the sample with different acid soaking time (i.e., different degrees of chemical damage) are compared with the simulated results. **Figure 7(b)** shows that the strain-stress responses of our model fit well with experimental data. It is worth noting that our model of cohesive bond does not consider the compaction hardening process at the initial stage. Hence, the calculated strain-stress responses before the peak are straight lines, different from concaved curves of experimental data. With the increasing soaking time, the pore volume increases, leading to elastic modulus decreases and pre-peak strain becoming larger. Our model can successfully describe this phenomenon.

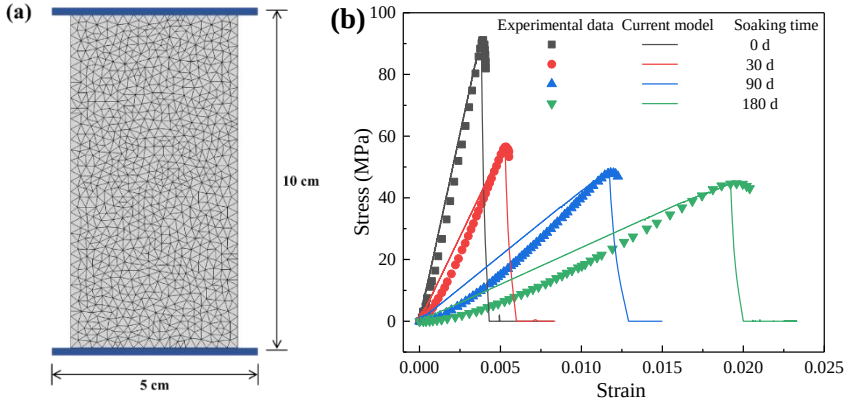

Figure 7: (a) Grid of sample prepared for uniaxial compression simulation of acid-corroded sandstone. (b) The stress-strain responses under different soaking times, which are obtained from experimental data of Li et al. (S. Li et al., 2021) **and simulation results of the proposed model.**

4. THMC COUPLED ROCK DISSOLUTION

This section discusses the THMC coupled pore-scale rock dissolved process (see Section 2.5) using the proposed model. The thermophysical parameters of fluid and solid, reaction parameters , and discrete parameters are listed in **Table 2**. Higher viscosity and diffusion coefficients are adopted to save computational cost and ensure numerical stability in LBM. However, the dimensionless parameters such as Prandtl number and Fourier number are maintained at the reality to ensure realistic simulation results, which is a commonly used approach in LBM. The rock is regarded as limestone, and its DEM mechanical parameters are also taken from **Table 1** because sandstone and limestone have similar mechanical properties(Jaeger et al., 2007). Reaction parameters are taken from the reaction of $CaCO_3$ with HCl (Portier & Vuataz, 2010). The lattice mesh is 2000×1400 with a lattice cell size of 5×10^{-5} m. Three *Da* (1.5×10^{-5}, 1.5×10^{-3}, 1.5) and three $P_{f,in}$ (10 MPa, 20 MPa, 30 MPa), a total of nine conditions will be discussed.

Table 2 Parameters related to THMC coupled rock dissolution.

Type	Parameter	Value
Fluid	Density ρ_f	1000 kg/m^3
	Heat capacity $\left(c_p\right)_f$	4.00 kJ/(kg·°C)
	Kinematic viscosity μ_f/ρ_f	2.20×10^{-3} m^2/s
	Thermal diffusion coefficient κ_f	1.40×10^{-3} m^2/s
	Solute diffusivity D_{L1} and D_{L2}	5.00×10^{-4} m^2/s
Solid	Density ρ_s	2500 kg/m^3

	Heat capacity $\left(c_p\right)_s$	1.00 kJ/(kg·°C)
	Thermal diffusion coefficient κ_s	3.50×10^{-3} m^2/s
	Factor of fracture fluid pathway c_d	0.2
Reaction	Molar volume of solid M_{S1}	4.03×10^{-5} m^3/mol
	Activation energy of energy E_a	62.80 kJ/mol
	Reference temperature T_0	237.15 K
	Effective equilibrium constant K_{eq}	1×10^{7}
	Reactant concentration at inlet $C_{L1,in}$	3 mol/L
Discretization	Lattice cell size	5×10^{-5} m
	DEM time step Δt_{DEM}	2.86×10^{-9} s
	LBM time step Δt_{LBM}	1×10^{-7} s
	Relaxation parameter of solute transport τ_h	0.7

4.1 Three types of THMC coupled rock dissolution

Figure 8 shows the concentration distribution of reactant $L1$ at the simulation time $5.6\times10^{7}\,\Delta t_{DEM}$. According to the dissolution morphology, the nine working conditions can be divided into three types: i) Permeation type for Da=1.5×10^{-5}, 1.5×10^{-3} and all injected pressures; ii) Cavity type for Da=1.5 and $P_{f,in}$=10 MPa and 20 MPa; iii) Permeation-cavity type for Da=1.5 and $P_{f,in}$=30 MPa. The following will discuss the THMC coupled mechanisms based on these three types.

i) Permeation type is in the case of small Da. Because the dissolution rate at the reactive surface is slow, there is always enough reactant added to the reactive surface, which is called a reaction-controlled process. The high injected pressure leads to high flow velocity in the fluid pathway. The flow velocity significantly determines the spread of reactant while having a weak effect on rock dissolution near the injection hole. This point is more obvious for Da=1.5×10^{-5} than for Da=1.5×10^{-3}, and so the spread range of reactant is larger for Da=1.5×10^{-5}. In other words, under the condition of smaller Da and higher flow velocity, the reactant spreads more widely, and the dissolution proceeds more uniformly inside the rock. This phenomenon was also reflected in the three dimensional hydro-chemical simulation analysis of Liu et al. (Liu & Mostaghimi, 2017) and the experimental observation of Menke et al. (Menke et al., 2015). The higher injected pressure makes the effect of hydraulic fracturing more obvious, and the greater Da makes the effect of chemical damage more obvious. Hence, more branched cracks and more complex fracture geometry falls at the intersection of high injected pressure and large Da, as presented in **Figure 9**. For hydrothermal characteristics, **Figure 10** shows that the pressure drop of the permeation type is concentrated around the injection hole, while the pressure drop inside the rock is no obvious. It indicates that the increase of fluid conductivity of rock is insignificant. The pressure response propagates uniformly around the injection hole, but only father along the crack direction. The pattern of temperature response of permeation type is similar to the pressure response, only propagating farther along the crack direction, as shown in **Figure 11**.

ii) Cavity type is in the case of large Da and small injected pressure. In this situation, the dissolution rate at the reactive surface is rapid, and the reactants near the surface are consumed quickly. However, due to the low flow velocity, the reactant cannot be timely supplied to the reactive surface, called the diffusion-controlled process. In the process of transportation, once the reactant encounters solid, it will be consumed. The dissolution hardly penetrates inside the rock and induces the cavity around the injection hole, as shown in **Figure 8**. Liu et al. (Liu & Mostaghimi, 2017) also found this phenomenon in their three-dimensional simulation results. Another feature is the distinct concentration-gradient inside the cavity, indicating that solute diffusion is dominant. **Figure 9** shows that there is no complex fracture geometry generated for the cavity type. For hydrothermal characteristics, high pressure accumulates inside the cavity, and the pressure drop is significant inside the rock compared with the permeation-type (see **Figure 10**). Accordingly, the pressure response area of the cavity type is larger than the permeation type, the same as the temperature response area (see **Figure 11**).

iii) Permeation-cavity type is in the case of large Da and high injected pressure. The rock dissolution is cavity type at the main fracture and around the injection hole, while it becomes permeation type at the secondary fractures. In this situation, both hydraulic fracturing and chemical damage realize their full potential. A complex and dense fracture network is formed, as shown in **Figure 9**. The fluid conductivity of rock increases significantly, and the pressure response can propagate further, as presented in **Figure 10**. Because the flow velocity inside the flow pathway is large, the temperature also spreads farther. **Figure 11** shows that the cooling area of rock is much larger than in other working conditions.

Overall, the three types have distinct differences in THMC physical response. Our model can correctly describe the process of rock dissolution and capture the detailed THMC coupled information.

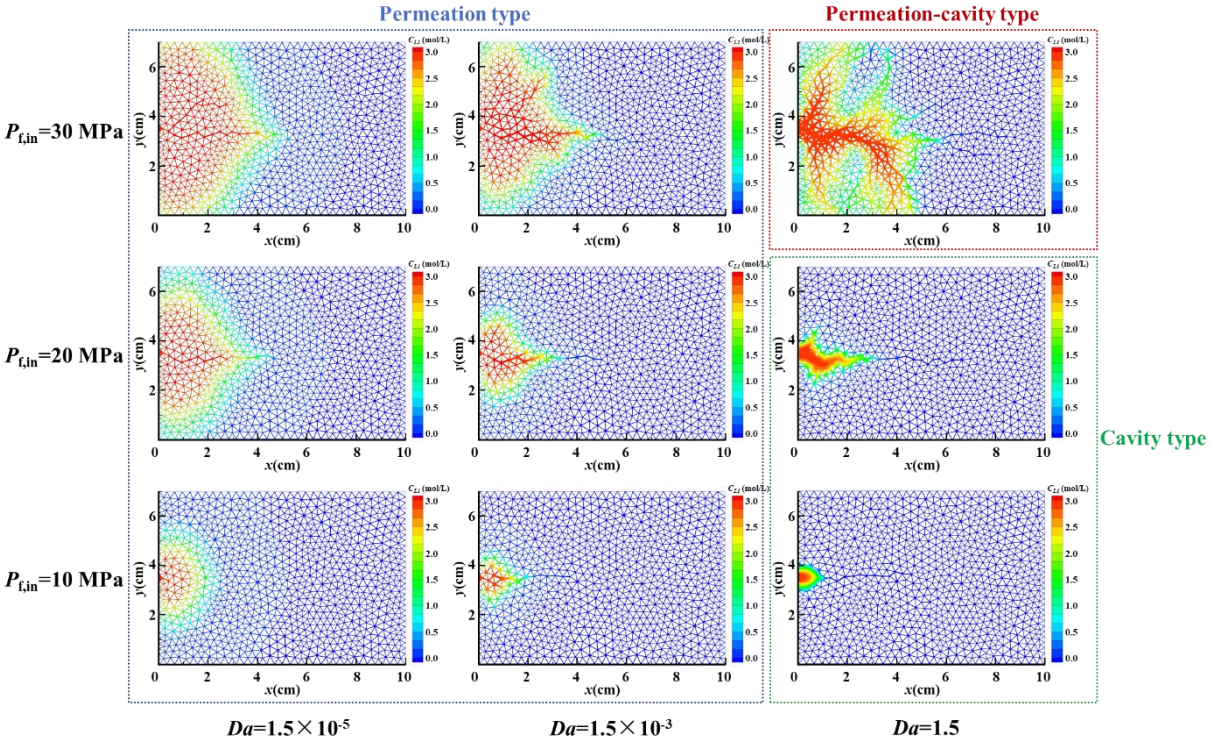

Figure 8: Simulation results of concentration distribution of reactant *L*1 with various injected pressure and *Da*, where the simulation time is 5.6×10^7 Δt_{DEM}.

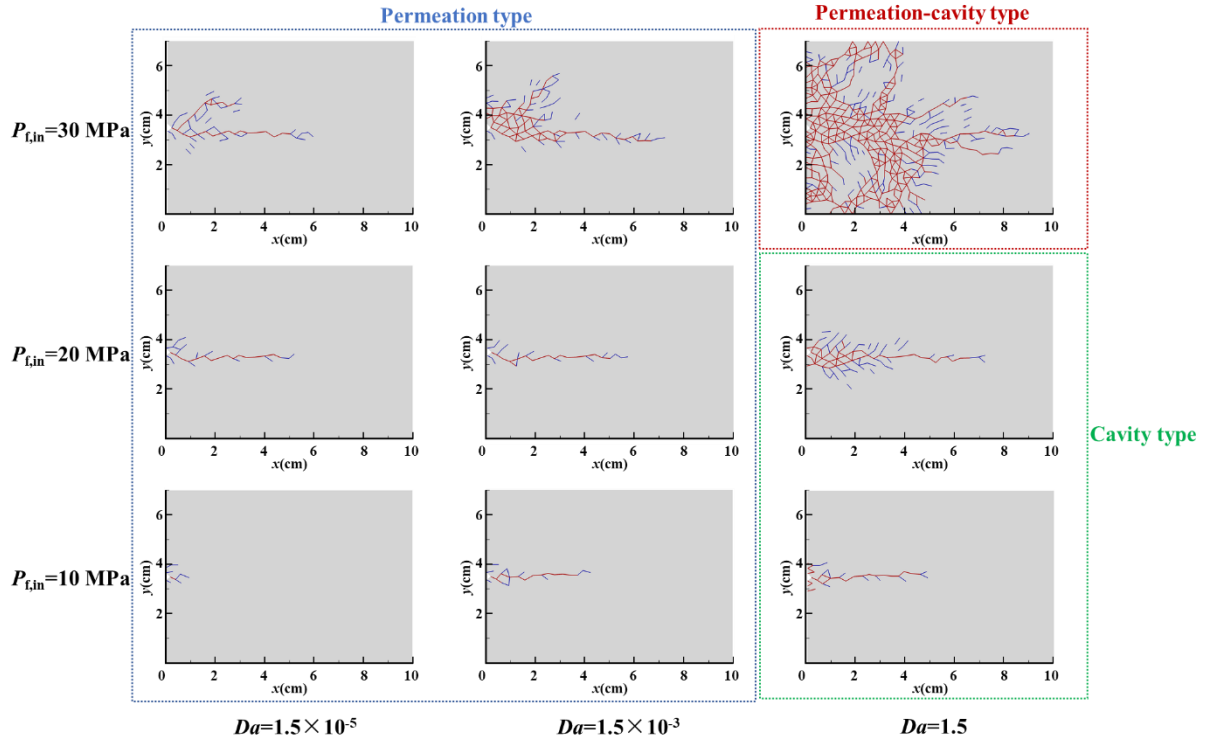

Figure 9: Simulation results of fracture geometry in rocks with various injected pressure and *Da*, where the simulation time is 5.6×10^7 Δt_{DEM}. Red line segments represent the failure of cohesive bond, and blue line segments represent cohesive bonds staying in the mechanical damage stage.

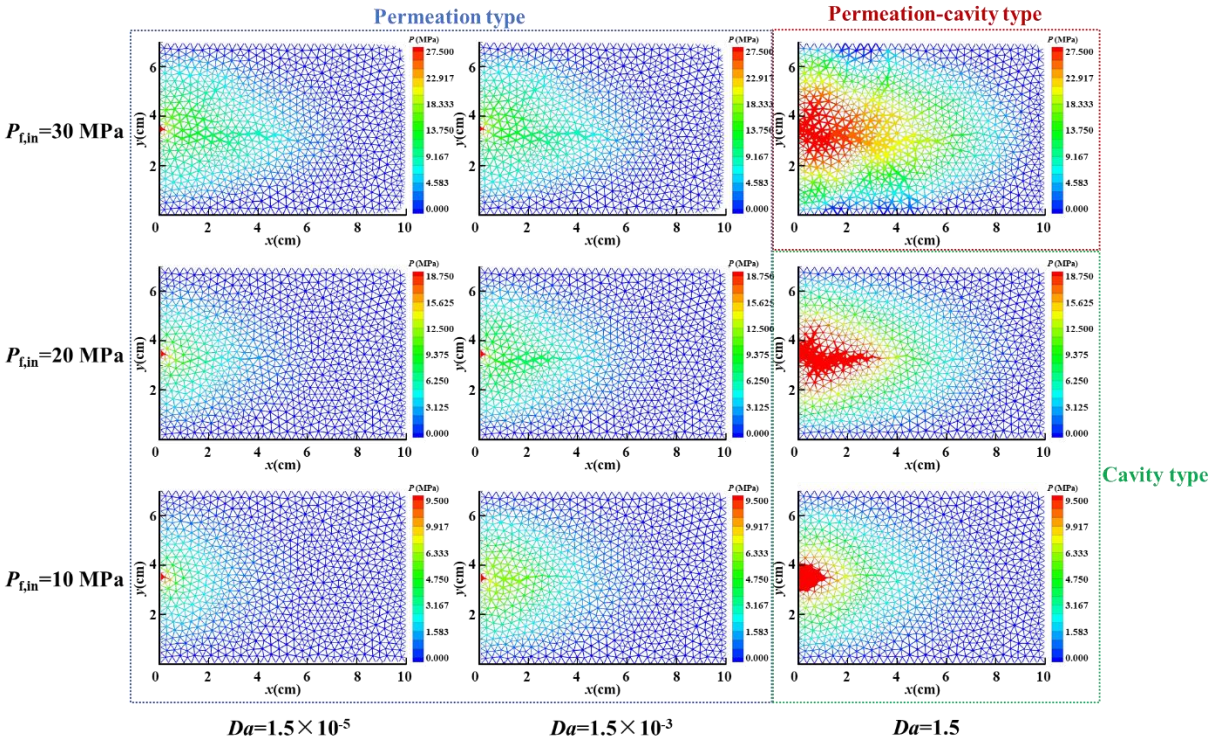

Figure 10: Simulation results of pressure distribution in rocks with various injected pressure and *Da*, where the simulation time is 5.6×10^7 Δt_{DEM}.

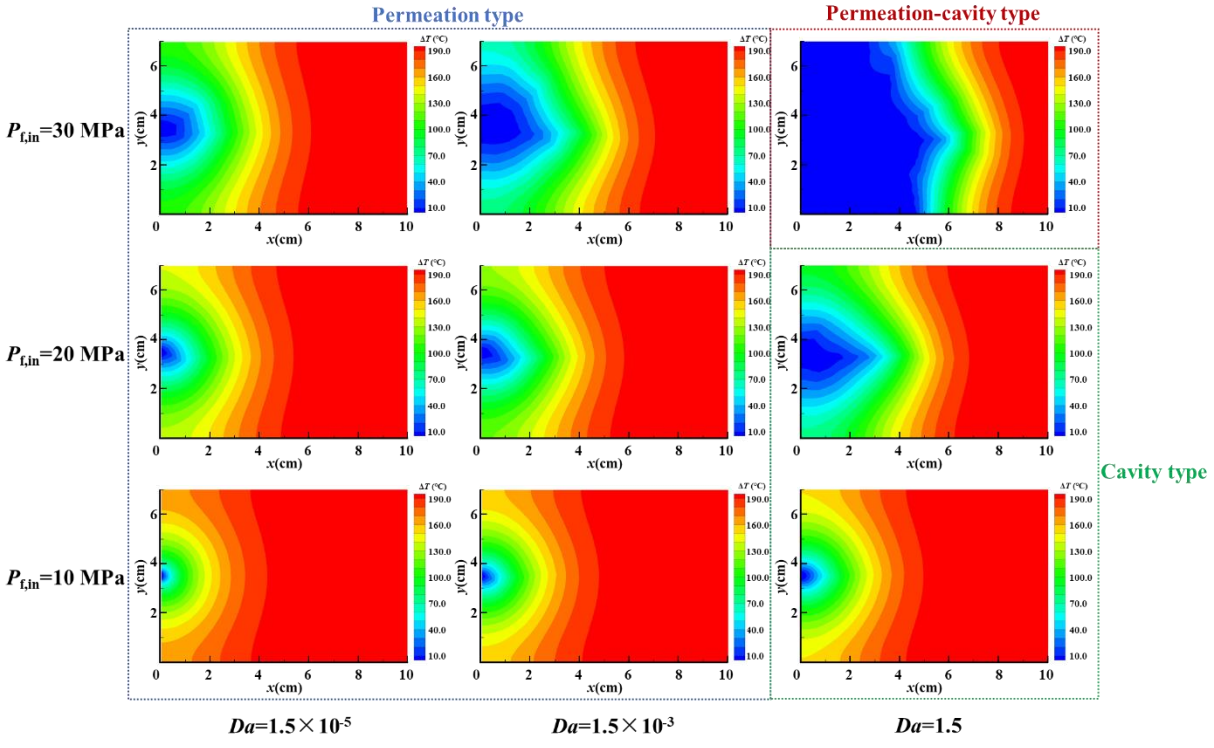

Figure 11: Simulation results of temperature change in rocks with various injected pressure and *Da*, where the simulation time is 5.6×10^7 Δt_{DEM}.

4.2 Evolution Characteristics of Reactive Surface Area

The evolution of reactive surface area with time is shown in **Figure 12**. All the working conditions present the continuous growth of the reactive surface area. However, the growth pattern is different in different rock dissolution types.

For the i) permeation type, the increasing rate of the reactive area is fast first and then slow down for Da=1.5×10^{-5}, or fast first and then nearly constant for Da=1.5×10^{-3}. The reason is explained as follows: the increasing reactive surface area has a close association with flow velocity when Da is small, and the flow velocity is closely related to the rock damage and fracture distribution. At the initial stage of injection, there is generation of rock damage and fractures around the injection hole under the influence of hydraulic fracturing. The flow velocity near the injection hole is high, the reactants are transported rapidly, and so the increasing rate of the reactive area is fast. With the accumulation of time, the reactant is transported far from the injection hole, and there are fewer fractures for flow. The flow velocity dependent on the initial fluid pathway is low, so the reactive surface area increases slowly.

For the ii) cavity type, the increasing rate of the reactive surface area is slow at first and then fast. This is because the increasing cavity enhances the fluid conductivity near the injection hole, so the fluid injection rate increases under the constant injected pressure. With time accumulation, a higher fluid injection rate corresponds to a higher reactant injection rate. For the diffusion-controlled process, the reactant mass in the cavity determines the dissolution rate, so the increasing rate of reactive surface area increases with time.

For the iii) permeation-cavity type, the increasing rate of the reactive surface area is slow at first, then fast, and then slow down again. The reason for this phenomenon can be simply undertint as follows: the main fracture is generated at the initial stage, and the rock dissolution first presents a cavity type at the main fracture and around the injection hole. Hence, the evolution of the increasing rate of reactive surface area follows the cavity type at the initial stage. Over the simulation time goes, the secondary fractures emerge, and the reactant propagates deeper inside the rock. Then, rock dissolution tends to show permeation type. **Figure 13** can describe this process.

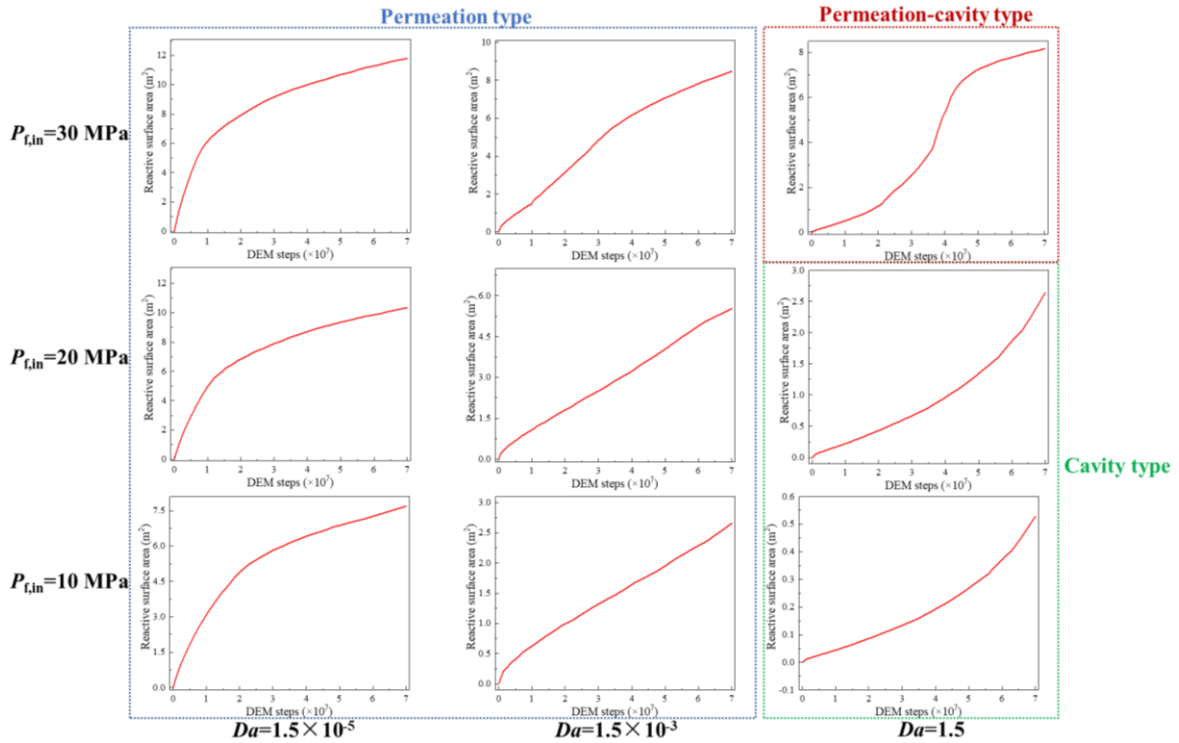

Figure 12: Evolution of reactive surface area in rocks with time under various injected pressure and *Da*.

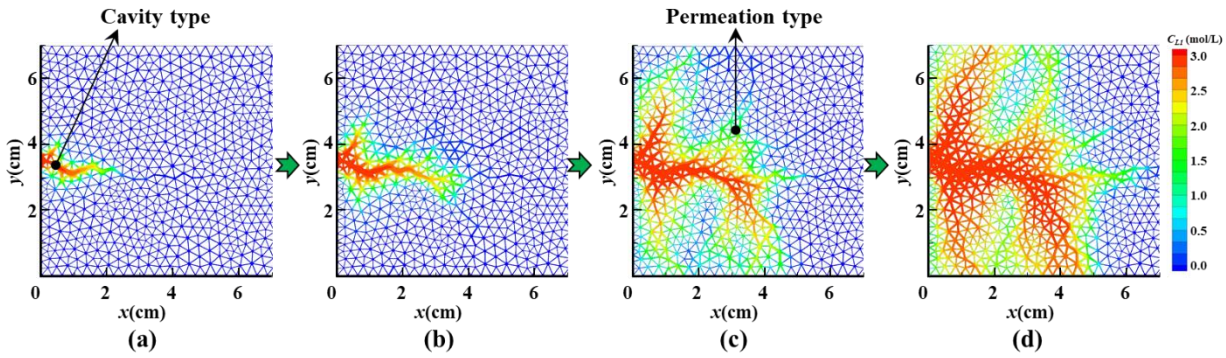

Figure 13: Evolution of concentration distribution of reactant with injected pressure 30 MPa and *Da*=1.5, where the simulation time is (a) 1.54×10^7 Δt_{DEM}, (b) 3.08×10^7 Δt_{DEM}, (c) 4.62×10^7 Δt_{DEM}, and (d) 7.00×10^7 Δt_{DEM}.

5. CONCLUSIONS

In the present work, a pore-scale THMC coupled model for the rock dissolution and fracturing process is developed firstly based on the method of combing the LBM and DEM. This model conducts a comprehensive THMC coupled scheme, especially rock dissolution, solute transport, and chemical damage. The chemical damage variable based on the cohesive bond is proposed to reflect the effect of rock dissolution on mechanical characteristics, including elastic modulus, strength, and critical fracture energy. The LB solute transport model and VOP method are adopted to describe the variation of fracture fluid pathways caused by rock dissolution. Two cases based on the analytical solution and experiment are used to verify the solute transport and chemical damage, respectively.

The THMC coupled acid fracturing is analyzed using the proposed model. The role of injected pressure and *Da* are particularly analyzed. The main findings can be summarized as follows: 1) Three types can be divided according to the dissolution morphology, they are permeation type (small *Da*), cavity type (large Da and small injected pressure), and permeation-cavity type (large *Da* and large injected pressure). THMC response characteristics are significantly different in three types. For the permeation-cavity type, the rock dissolution around the main fracture is cavity type, while there is a permeation type around the secondary fractures. 2) The increasing pattern of reactive surface area with time is different in different rock dissolution types. For the permeation type, the increasing rate of the reactive area is fast at first and then slows down or is nearly unchanged. For the cavity type, the increasing rate of reactive surface area is slow at first and then fast. The permeation-cavity type shows a separate cavity type and permeation type in time sequence.

ACKNOWLEDGEMENTS

The study is supported by the National Natural Science Foundation of China (No. 51936001) and Scientific Research Project of Beijing Educational Committee (KZ202110017026).

REFERENCES

Boutt, D., Cook, B., & Williams, J. (2011). A coupled fluid–solid model for problems in geomechanics: Application to sand production. *International Journal for Numerical and Analytical Methods in Geomechanics*, *35*(9), 997–1018. https://doi.org/10.1002/nag.938

Caulk, R., & Chareyre, B. (2019). An open framework for the simulation of coupled Thermo-Hydro-Mechanical processes in Discrete Element Systems. In *The 8th International Conference on Discrete Element Methods*. Enschede, Netherlands.

Caulk, R., Sholtès, L., Krzaczek, M., & Chareyre, B. (2020). A pore-scale thermo–hydro-mechanical model for particulate systems. *Computer Methods in Applied Mechanics and Engineering*, *372*, 113292. https://doi.org/10.1016/j.cma.2020.113292

Chen, L., Luan, H. B., He, Y. L., & Tao, W. Q. (2012). Pore-scale flow and mass transport in gas diffusion layer of proton exchange membrane fuel cell with interdigitated flow fields. *International Journal of Thermal Sciences*, *51*(1), 132–144. https://doi.org/10.1016/j.ijthermalsci.2011.08.003

Chen, L., Kang, Q., Carey, B., & Tao, W. Q. (2014). Pore-scale study of diffusion-reaction processes involving dissolution and precipitation using the lattice Boltzmann method. *International Journal of Heat and Mass Transfer*, *75*, 483–496. https://doi.org/10.1016/j.ijheatmasstransfer.2014.03.074

Chen, L., Kang, Q., Viswanathan, H., & Tao, W. (2014). Pore-scale study of dissolution-induced changes in hydrologic properties of rocks with binary minerals. *Water Resources Research*, *50*(12), 9343–9365. https://doi.org/10.1002/2014WR015646

Chen, Y., Xiao, P., Du, X., Wang, S., Fernandez-Steeger, T. M., & Azzam, R. (2021). Study on damage constitutive model of rock under freeze-thaw-confining pressure-acid erosion. *Applied Sciences (Switzerland)*, *11*(20). https://doi.org/10.3390/app11209431

Chen, Z., & Wang, M. (2017). Pore-scale modeling of hydromechanical coupled mechanics in hydrofracturing process. *Journal of Geophysical Research: Solid Earth*, *122*(5), 3410–3429. https://doi.org/10.1002/2017JB013989

Huang, Z., Zeng, W., Wu, Y., Li, S., Gu, Q., & Zhao, K. (2021). Effects of temperature and acid solution on the physical and tensile mechanical properties of red sandstones. *Environmental Science and Pollution Research*, *28*(16), 20608–20623. https://doi.org/10.1007/s11356-020-11866-x

Jaeger, J. C., W.cook, N. G., & Zimmerman, R. W. (2007). *Fundamentals of Rock Mechanics*. *Geofluids* (Fourth edi, Vol. 9). Blackwell Publishing. https://doi.org/10.1111/j.1468-8123.2009.00251.x

Ji, S., & Tian, Y. (2021). Numericla ice tank for ice loads based on multi-media and multi-scale discrete elment method. *Chinise Journal of Theoretical and Applied Mechanics*, *53*(9), 27.

Jiao, K., Han, D., Li, J., Bai, B., Gong, L., & Yu, B. (2021). A novel LBM-DEM based pore-scale thermal-hydro-mechanical model for the fracture propagation process. *Computers and Geotechnics*, *139*, 104418. https://doi.org/10.1016/j.compgeo.2021.104418

Jiao, K., Han, D., Wang, D., Chen, Y., Li, J., Gong, L., et al. (2022). Investigation of thermal-hydro-mechanical coupled fracture propagation considering rock damage. *Computational Geosciences*. https://doi.org/10.1007/s10596-022-10155-5

Jin, S., Wang, X., Wang, Z., Mo, S., Zhang, F., & Tang, J. (2021). Evaluation Approach of Rock Brittleness Index for Fracturing Acidizing Based on Energy Evolution Theory and Damage Constitutive Relation. *Lithosphere*, *2021*(Special Issue 4), 1–18. https://doi.org/10.2113/2021/2864940

Kang, Q., Lichtner, P. C., Viswanathan, H. S., & Abdel-Fattah, A. I. (2010). Pore scale modeling of reactive transport involved in geologic CO2 sequestration. *Transport in Porous Media*, *82*(1), 197–213. https://doi.org/10.1007/s11242-009-9443-9

Krüger, T., Kusumaatmaja, H., Kuzmin, A., Shardt, O., Silva, G., & Viggen, E. M. (2016). *The Lattice Boltzmann Method - Principles and Practice*. Springer. https://doi.org/10.1007/978-3-319-44649-3

Krzaczek, M., Nitka, M., & Tejchman, J. (2021). Effect of gas content in macropores on hydraulic fracturing in rocks using a fully coupled DEM/CFD approach. *International Journal for Numerical and Analytical Methods in Geomechanics*, *45*(2), 234–264. https://doi.org/10.1002/nag.3160

Li, S., Huo, R., Wang, B., Ren, Z., Ding, Y., Qian, M., & Qiu, T. (2018). Experimental Study on Physicomechanical Properties of Sandstone under Acidic Environment. *Advances in Civil Engineering*, *2018*. https://doi.org/10.1155/2018/5784831

Li, S., Wu, Y., Huo, R., Song, Z., Fujii, Y., & Shen, Y. (2021). Mechanical Properties of Acid-corroded Sandstone Under Uniaxial Compression. *Rock Mechanics and Rock Engineering*, *54*(1), 289–302. https://doi.org/10.1007/s00603-020-02262-5

Li, W., Soliman, M., & Han, Y. (2016). Microscopic numerical modeling of Thermo-Hydro-Mechanical mechanisms in fluid injection process in unconsolidated formation. *Journal of Petroleum Science and Engineering*, *146*, 959–970. https://doi.org/10.1016/j.petrol.2016.08.010

Lisjak, A., & Grasselli, G. (2014). A review of discrete modeling techniques for fracturing processes in discontinuous rock masses. *Journal of Rock Mechanics and Geotechnical Engineering*, *6*(4), 301–314. https://doi.org/10.1016/j.jrmge.2013.12.007

Liu, M., & Mostaghimi, P. (2017). Pore-scale simulation of dissolution-induced variations in rock mechanical properties. *International Journal of Heat and Mass Transfer*, *111*, 842–851. https://doi.org/10.1016/j.ijheatmasstransfer.2017.04.049

Meng, X., & Guo, Z. (2016). Localized lattice Boltzmann equation model for simulating miscible viscous displacement in porous media. *International Journal of Heat and Mass Transfer*, *100*, 767–778. https://doi.org/10.1016/j.ijheatmasstransfer.2016.04.095

Menke, H. P., Bijeljic, B., Andrew, M. G., & Blunt, M. J. (2015). Dynamic three-dimensional pore-scale imaging of reaction in a carbonate at reservoir conditions. *Environmental Science and Technology*, *49*(7), 4407–4414. https://doi.org/10.1021/es505789f

Pathak, H., Singh, A., Singh, I. V., & Yadav, S. K. (2015). Fatigue crack growth simulations of 3-D linear elastic cracks under thermal load by XFEM. *Frontiers of Structural and Civil Engineering*, *9*(4), 359–382. https://doi.org/10.1007/s11709-015-0304-z

Portier, S., & Vuataz, F. D. (2010). Developing the ability to model acid-rock interactions and mineral dissolution during the RMA stimulation test performed at the Soultz-sous-Forêts EGS site, France. *Comptes Rendus - Geoscience*. https://doi.org/10.1016/j.crte.2010.04.002

Ramstad, T., Berg, C. F., & Thompson, K. (2019). Pore-Scale Simulations of Single- and Two-Phase Flow in Porous Media: Approaches and Applications. *Transport in Porous Media*, *130*(1), 77–104. https://doi.org/10.1007/s11242-019-01289-9

De Schutter, G. (2002). Finite element simulation of thermal cracking in massive hardening concrete elements using degree of hydration based material laws. *Computers and Structures*, *80*(27–30), 2035–2042. https://doi.org/10.1016/S0045-7949(02)00270-5

Shi, G., & Goodman, R. (1988). Discontinuous deformation analysis e a new method for computing stress, strain and sliding of block systems. In *the 29th US Symposium on Rock Mechanics*. Rotterdam: A.A. Balkema.

Shovkun, I., & Espinoza, D. N. (2019). Fracture Propagation in Heterogeneous Porous Media: Pore-Scale Implications of Mineral Dissolution. *Rock Mechanics and Rock Engineering*. https://doi.org/10.1007/s00603-019-01766-z

Sullivan, S. P., Sani, F. M., Johns, M. L., & Gladden, L. F. (2005). Simulation of packed bed reactors using lattice Boltzmann methods. *Chemical Engineering Science*, *60*(12), 3405–3418. https://doi.org/10.1016/j.ces.2005.01.038

Tahmasebi, P., & Kamrava, S. (2019). A pore-scale mathematical modeling of fluid-particle interactions: Thermo-hydro-mechanical coupling. *International Journal of Greenhouse Gas Control*, *83*(July 2018), 245–255. https://doi.org/10.1016/j.ijggc.2018.12.014

Wang, L., Wang, S., Zhang, R., Wang, C., Xiong, Y., Zheng, X., et al. (2017). Review of multi-scale and multi-physical simulation technologies for shale and tight gas reservoirs. *Journal of Natural Gas Science and Engineering*, *37*, 560–578. https://doi.org/10.1016/j.jngse.2016.11.051

Wu, Z., Zhou, Y., Weng, L., Liu, Q., & Xiao, Y. (2020). Investigation of thermal-induced damage in fractured rock mass by coupled FEM-DEM method. *Computational Geosciences*, *24*(5), 1833–1843. https://doi.org/10.1007/s10596-020-09970-5

Xu, H., Cheng, J., Zhao, Z., Lin, T., Liu, G., & Chen, S. (2021). Coupled thermo-hydro-mechanical-chemical modeling on acid fracturing in carbonatite geothermal reservoirs containing a heterogeneous fracture. *Renewable Energy*, *172*, 145–157. https://doi.org/10.1016/j.renene.2021.03.023

Xu, T. (n.d.). *THM coupling process in unsatureated bentonite buffer material with construction joints and self-heating effects*. Beijing Jiaotong University. Retrieved from 10.26944/d.cnki.gbfju.2019.000770

Yan, C., Xie, X., Ren, Y., Ke, W., & Wang, G. (2022). A FDEM-based 2D coupled thermal-hydro-mechanical model for multiphysical simulation of rock fracturing. *International Journal of Rock Mechanics and Mining Sciences*, *149*(January), 104964. https://doi.org/10.1016/j.ijrmms.2021.104964

Zhang, R., Yin, X., Winterfeld, P. H., & Wu, Y.-S. (2016). A fully coupled thermal-hydrological-mechanical-chemical model for CO2 geological sequestration. *JOURNAL OF NATURAL GAS SCIENCE AND ENGINEERING*, *28*, 280–304. https://doi.org/10.1016/j.jngse.2015.11.037

Zhang, T., Shi, B., Guo, Z., Chai, Z., & Lu, J. (2012). General bounce-back scheme for concentration boundary condition in the lattice-Boltzmann method. *Physical Review E - Statistical, Nonlinear, and Soft Matter Physics*, *85*(1), 1–14. https://doi.org/10.1103/PhysRevE.85.016701

Zhang, W., Guo, T. kui, Qu, Z. qing, & Wang, Z. (2019). Research of fracture initiation and propagation in HDR fracturing under thermal stress from meso-damage perspective. *Energy*, *178*, 508–521. https://doi.org/10.1016/j.energy.2019.04.131

Zhou, S., Liu, D., Cai, Y., Yao, Y., & Li, Z. (2017). 3D characterization and quantitative evaluation of pore-fracture networks of two Chinese coals using FIB-SEM tomography. *International Journal of Coal Geology*, *174*(March), 41–54. https://doi.org/10.1016/j.coal.2017.03.008

Zhou, X., Xu, Z., Xia, Y., Li, B., & Qin, J. (2020). Pore-scale investigation on reactive flow in porous media with immiscible phase using lattice Boltzmann method. *Journal of Petroleum Science and Engineering*, *191*, 107224. https://doi.org/10.1016/j.petrol.2020.107224